energies

MDPI

Article

A Bidirectional Grid-Connected DC–AC Converter for Autonomous and Intelligent Electricity Storage in the Residential Sector

Ismail Aouichak, Sébastien Jacques *, Sébastien Bissey, Cédric Reymond, Téo Besson and Jean-Charles Le Bunetel

Research Group on Materials, Microelectronics, Acoustics, and Nanotechnology, GREMAN UMR 7347, University of Tours, CNRS, INSA Centre Val-de-Loire, 37100 Tours, France; ismail.aouichak@univ-tours.fr (I.A.); sebastien.bissey@univ-tours.fr (S.B.); cedric.reymond@st.com (C.R.); teo.besson@univ-tours.fr (T.B.); lebunetel@univ-tours.fr (J.-C.L.B.)

* Correspondence: sebastien.jacques@univ-tours.fr; Tel.: +33-6-667-639-46

Abstract: Controlling the cost of electricity consumption remains a major concern, particularly in the residential sector. Smart home electricity management systems (HEMS) are becoming increasingly popular for providing uninterrupted power and improved power quality, as well as for reducing the cost of electricity consumption. When power transfer is required between a storage system and the AC grid, and vice versa, these HEMS require the use of a bidirectional DC–AC converter. This paper emphasizes the potential value of an almost unexplored topology, the design of which was based on the generation of sinusoidal signals from sinusoidal half waves. A DC–DC stage, which behaved as a configurable voltage source, was in series with a DC–AC stage, i.e., an H-bridge, to achieve an architecture that could operate in both grid and off-grid configurations. Wide bandgap power switches (silicon carbide metal-oxide-semiconductor field-effect transistors [MOSFETs]), combined with appropriate control strategies, were the keys to increasing compactness of the converter while ensuring good performance, especially in terms of efficiency. The converter was configured to automatically change the operating mode, i.e., inverter or rectifier in power factor correction mode, according to an instruction issued by the HEMS; the latter being integrated in the control circuit with automatic duty cycle management. Therefore, the HEMS set the amount of energy to be injected into the grid or to be stored. The experimental results validate the operating modes of the proposed converter and demonstrate the relevance of such a topology when combined with an HEMS, especially in the case of an AC grid connection. The efficiency measurements of the bidirectional DC–AC converter, performed in grid-connected inverter mode, show that we exceeded the efficiency target of 95% over the entire output power range studied, i.e., from 100 W to 1.5 kW.

Keywords: home electricity management systems; bidirectional DC–AC converter; high compactness; high efficiency

Citation: Aouichak, I.; Jacques, S.; Bissey, S.; Reymond, C.; Besson, T.; Le Bunetel, J.-C. A Bidirectional Grid-Connected DC–AC Converter for Autonomous and Intelligent Electricity Storage in the Residential Sector. *Energies* **2022**, *15*, 1194. https://doi.org/10.3390/en15031194

Academic Editors: Massimiliano Luna and Nicu Bizon

Received: 2 November 2021
Accepted: 4 February 2022
Published: 7 February 2022

1. Introduction

The energy policy challenges facing the European Union are greater than ever. One such challenge is the intelligent management of electricity at all levels, from production to final consumption [1,2]. Distribution efficiency and the reliability of service delivery are two indicators that can be used to evaluate the performance of distribution systems [3,4]. The increasing deployment of smart grids has improved their monitoring and controllability [5]. An example of a modern smart grid feature is the ability to assist with load shifting, limit peak demand and automatically identify malfunctions or outages [6]. These issues are all the more controversial as the number of microgrids, i.e., small-scale independent power systems, continues to grow. Two main modes of operation characterize a microgrid: the grid-connected mode and the off-grid mode [7]. In off-grid mode, electricity is either

unavailable due to a grid failure or outage, or the power grid is in islanding mode, i.e., completely inaccessible. The performance of standalone microgrids has been regularly analyzed in the literature for several years. These standalone microgrids typically consist of two key components: photovoltaic (PV) arrays and/or wind turbines and energy storage systems, such as flywheels, supercapacitors or batteries, which are used to implement intelligent voltage regulation and load tracking systems [8,9].

Energy management strategies are currently playing an increasingly important role in regulating the power quality of microgrids [10]. One of the challenges is to control energy flows to achieve various operational objectives, such as cost minimization, guaranteed delivery or security. One method to achieve this is to adjust the flow of energy to and from the main grid, the distribution of energy resources and the controllability of loads. In the residential sector, this type of strategy, now known as a home electricity management system (HEMS), is typically implemented to stimulate the integration of renewable energy and to protect the electricity distribution system from potential outages [11].

With the advent of Internet of things (IoT)-based smart buildings, in which all smart appliances are connected, as well as smart meters, we now have not only real-time usage data but also the ability to remotely operate various appliances in a home [12,13]. Much of this data can be used by an HEMS to improve the synchronization of energy transfers between the storage system, power generation and its consumption.

A wide range of techniques is already available in the literature and these techniques can be classified into two main categories [14–18]. Indeed, these approaches are based either on information processing methods or on optimization tactics:

- Information process methods: These methods are designed to model nonlinear systems. For example, HEMS controllers can use artificial intelligence (AI) methods, such as support vector machines (SVM), artificial neural networks (ANN) or recurrent neural networks (RNN), to map the electrical properties of the house using categorized metering data [19]. There are also adaptive neural fuzzy inference systems (ANFIS), which represent a mix of neural networks and fuzzy inference systems, to monitor and predict power consumption [20];
- Optimization process methods: These methods use fixed functions, such as economic feasibility, optimal management or error minimization. Model predictive control (MPC), particle swarm optimization (PSO) and genetic algorithm (GA) are three examples of the most commonly used techniques in HEMS scheduling [21,22].

As shown in Figure 1, Bissey et al. recently proposed an example of HEMS using fuzzy logic control (FLC) [23]. This approach used machine learning and data collected from different houses (i.e., time, day, past power consumption and indoor/outdoor temperature data) to find optimized criteria for the configuration of an HEMS. Although the approach described in this paper is effective, its validity only makes sense if a large experimental database is available to build the fuzzy rule base and membership functions needed to make this HEMS work. Recently emerged deep learning (DL) methods are proving to be effective tools, even surpassing traditional approaches as they greatly reduce the need for human interaction [24,25].

A storage system is required for the installation of such an HEMS. Alternating loads can be powered either directly from the AC grid or through an inverter in case the storage system would relieve the AC grid. To implement these two modes of operation, a necessarily bidirectional DC–AC converter must be operational [26]. Its metrics in terms of compactness, efficiency and output signal quality must be as high as possible. In this context and as illustrated in Figure 1, this paper focuses on the sizing and implementation of such a bidirectional converter.

Multilevel DC–AC converters, introduced in the 1980s, that are widely deployed today and whose performance has been discussed in the literature for many years allow the output voltage to be varied in steps by generating levels [27–29].

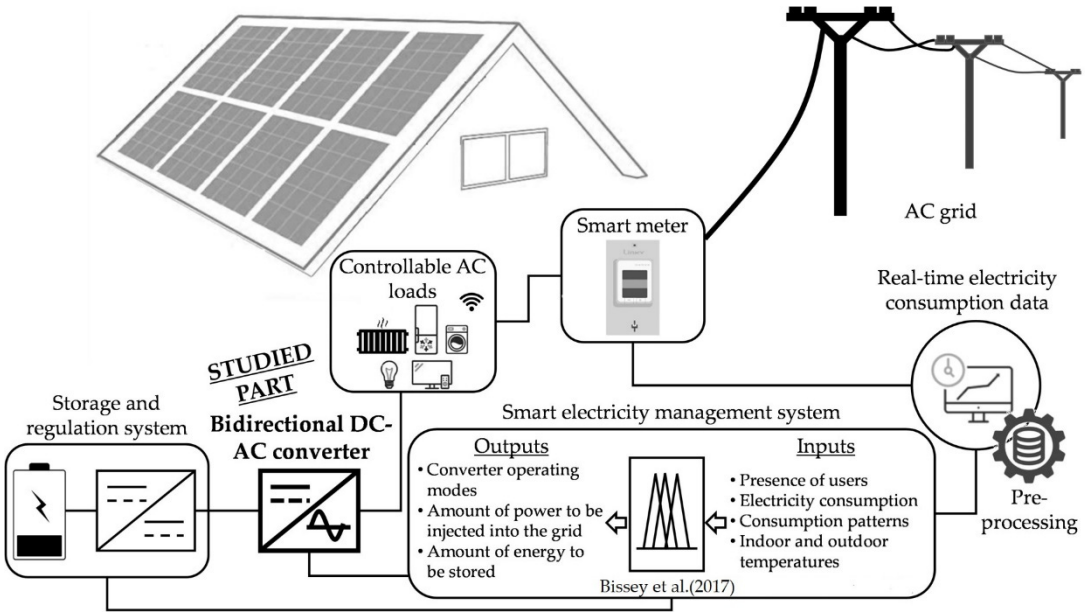

Figure 1. The principle of the smart HEMS implemented in this study [23].

By significantly increasing the number of levels, the output signals become more similar to sinusoids, which drastically reduces their total harmonic distortion (THD) and thus, improves the power quality of the converter and a fortiori of the microgrid. To increase the number of levels, two approaches are classically implemented: increasing the number of voltage sources on the DC bus side or multiplying the number of semiconductor devices to be controlled [30]. Multilevel converter topologies are still widely used for medium and high voltage applications, such as electrical motor drives or grid connected converters, because they generate very low harmonics [31].

Totem pole topologies are also interesting structures dedicated to bidirectional DC–AC conversion. In this type of structure, bidirectional switches based on MOSFETs, thyristors or Triacs are used. Such a topology is generally suitable for high-power applications. Its two main advantages are the reduction in the number of components to be controlled and the simplicity of the use of the converter itself. Recent studies have demonstrated their energy efficiency for particularly high-power densities [32,33].

Despite their high energy efficiency, totem pole topologies cause electromagnetic interference at high frequencies due to the floating points that exist in these architectures. Multilevel DC–AC topologies, widely used today in high voltage, use particularly bulky filters to limit electromagnetic compatibility problems. Thus, to avoid these problems, we sought to implement a topology more suitable for HEMS applications whilst remaining within the specified power range.

This paper aims to prove experimentally the merits of another type of bidirectional DC–AC converter that is more suitable for HEMS applications. The proposed topology, which has not yet been fully explored in the literature [34,35], is formed by the association in series of a DC–DC stage and a DC–AC stage with these two stages being necessarily bidirectional. In inverter mode, the DC–DC stage generates a full-wave rectified sine wave thanks to its pulse width modulation (PWM) control. This signal is then inverted half-period by half-period by the DC–AC stage to create the sine wave signal. In rectifier mode, the DC–AC stage acts as a full bridge while power factor correction (PFC) is provided by the DC–DC stage.

The main contribution of this study is the sizing and experimental validation of the proposed bidirectional DC–AC converter topology coupled with a control strategy for HEMS applications. This converter needed excellent compactness and high efficiency (at least 95%), both at low power (a few hundred watts) and up to 1.5 kW. The HEMS, which

is associated with the designed converter, needed to supervise the transition between operating modes, as well as the amount of energy stored or injected into the AC grid.

The remainder of this paper consists of the following sections. Section 2 describes the proposed topology with the above key properties. The sizing strategy of the converter and the main experimental results are presented in Section 3. Finally, a discussion based on the main experimental results that were obtained is proposed in Section 4.

2. Bidirectional DC–AC Converter Topology Proposal and Control Methodology

In order to validate the fuzzy logic-based control technique implemented in our proposed HEMS [23], we had to design a bidirectional DC–AC converter that was capable of functioning as both an inverter and a PFC rectifier. The transition between these two modes of operation needed to be fully automated and without human intervention in order for our HEMS to autonomously store, produce and supply energy for domestic use.

Before validating its operation by appropriate experimental measurements, it is essential to detail the operating modes of the converter, as well as its control strategies.

2.1. Proposed Topology and Details of Its Operating Modes

Figure 2 shows the overall structure of the proposed bidirectional DC–AC converter. The energy transfer between a DC voltage source and an AC voltage source, and vice versa, was the basis of this structure. The association in series of a DC–DC stage and a DC–AC stage ensured this principle of operation with these two stages being necessarily bidirectional.

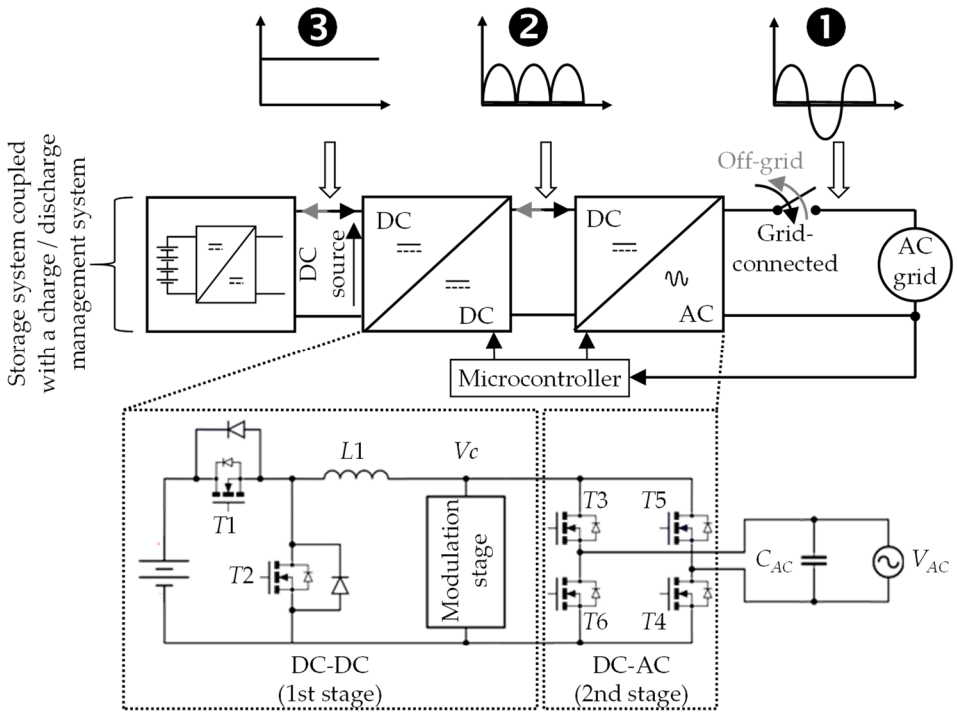

Figure 2. Principle diagram of the proposed bidirectional DC–AC converter.

The DC–DC stage needed to generate a rectified sine wave from the PWM command of the power switches (see ❷ in Figure 2). Since the power devices in this stage switched at a frequency of a few hundred kilohertz to optimize the compactness of the whole converter, the inductance, noted *L*1 in Figure 2, was sized so that the ripple of the current was negligible compared to the sinusoidal component at low frequency (in this case, 50 Hz). Therefore, the DC–DC converter acted as a controllable output voltage source.

By changing the voltage of a modulation stage, the output current could be regulated. This is very interesting, especially when the output current is strongly reduced or in the of variable DC voltage. This strategy allowed the output voltage of the DC–DC stage

to be modulated. Specifically, when this modulated voltage was higher than the mains voltage, the output current had a positive value. In the opposite case, the output current was negative.

Thus, two modes of operation were possible:

- Inverter mode: In this case, energy was transferred from the storage system to the AC grid (see the black arrows in Figure 2, as well as Figure 3).
- PFC rectifier mode: In this operating mode, energy was transferred from the AC grid to the storage system (see the grey arrows in Figure 2, as well as Figure 4).

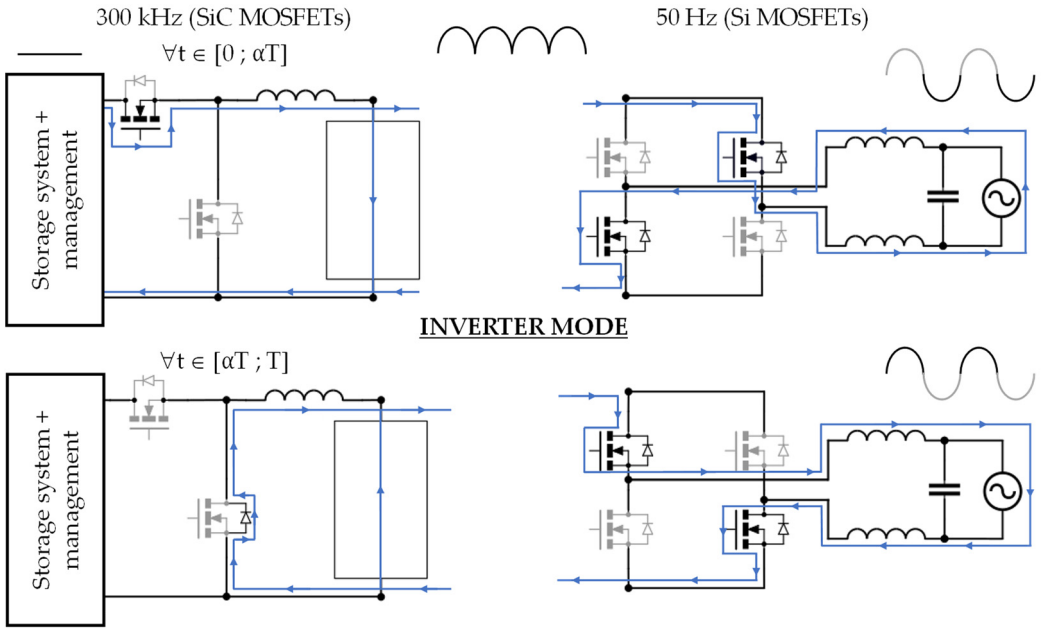

Figure 3. Schematic diagram of the converter in inverter mode.

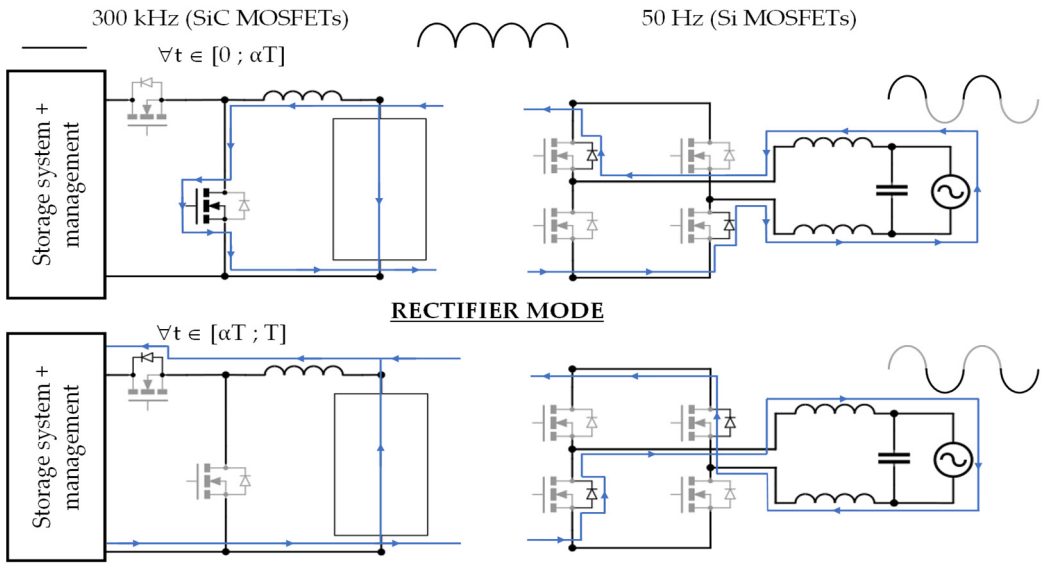

Figure 4. Schematic diagram of the converter in PFC rectifier mode.

The design approach that was chosen allowed the converter to be used in both grid-connected and off-grid modes. Since the microcontroller was synchronized with the AC grid to sensibly drive the DC–DC and DC–AC stages, only the grid-connected mode will be discussed in the remainder of this paper.

The DC–AC stage was responsible for inverting every other sinusoidal half-wave to obtain a full sinusoidal output signal (see ❶ in Figure 2).

Compared to existing voltage source converter topologies, such as multilevel structures, the coupling of a DC–DC stage with an H-bridge has many advantages:

- The standard DC–DC converter and the H-bridge are two very common and mastered topologies;
- Many H-bridge topologies are composed of four or more power components that switch at high frequency. In our proposed architecture, only those in the DC–DC stage (see transistors *T*1 and *T*2 in Figure 2) operated at high frequency, i.e., 150 kHz implemented here. In the DC–AC stage, all components (see components *T*3, *T*4, *T*5 and *T*6 in Figure 2) switched at low frequency, i.e., 50 Hz;
- When switching at high frequency, it is imperative to take into account the delay between the two switching operations in the same branch for safety reasons. Here, the safety delay was easier to regulate since only one stage operated at high frequency;
- In our architecture, the capacitance used at high frequency to modulate the voltage *Vc* (see Figure 2) was small (about 10 µF). This is not the case in many other topologies in the literature, where the authors consider that the use of an AC capacitor is mandatory.

2.2. Modulation of the Output Voltage of the DC–DC Stage

In a rather classical way, three solutions (see Figure 5) are proposed here to adjust the voltage *Vc* (see Figure 2) of the DC–DC stage. We assume that the whole DC–AC converter operates in inverter mode (see Figure 3) to briefly explain each solution.

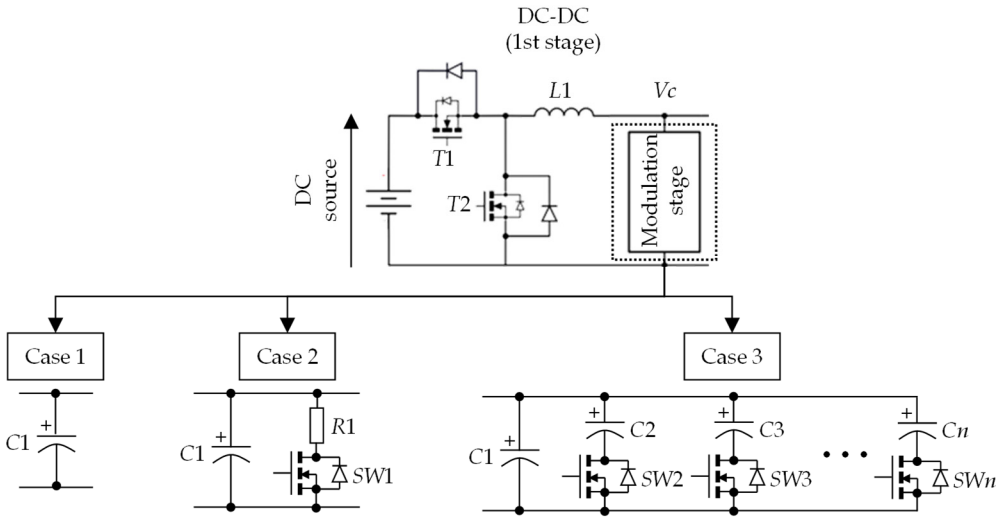

Figure 5. Solutions to modulate the output voltage of the DC–DC stage.

In the three cases of Figure 5, the output capacitor of the DC–DC stage, noted *C*1, was always used. Its value considered here was 10 µF to avoid a strong ripple of the voltage *Vc*.

The first solution (see Case 1 in Figure 5) was to use the capacitor *C*1 directly. The DC–DC stage then operated as a buck-type step-down converter. Despite the simplicity of this solution since it does not use any power device, it has a major drawback. Indeed, a current could flow inside the transistor, named *T*2 in Figure 2, during the discharge of the capacitor, which could lead to it overheating.

As can be seen in Case 2 in Figure 5, a resistor of a few ohms coupled with a switch could be used to solve the above problem. If the load impedance was too high, then the capacitor used in this case could be discharged through this resistor. This solution was especially interesting when the output power of the inverter fluctuated during operation. However, because of this resistance, this solution strongly penalized the efficiency of the DC–DC stage and, by extension, of the whole DC–AC converter.

The last solution (see Case 3 in Figure 5) was to connect n-quadrupoles in parallel. Each quadrupole consisted of a capacitor and a power switch that were in series. Such a solution aimed to fix the ripple of the output voltage of the DC–DC stage. Even though this solution was slightly more complex than the previous ones, adaptation to many more loads could be achieved. Finally, the efficiency of the DC–DC stage was not penalized so much in this case. In the remainder of this manuscript, this solution is implemented with two quadrupoles in parallel with the output capacitor (see capacitor $C1$ in Figure 5) of the DC–DC stage. In conclusion, the values of the three capacitors, $C1$, $C2$ and $C3$, of the modulation stage were equal to 10 µF, 1 µF and 68 nF, respectively (see Figure 5). The value of each capacitor was determined by the ripple of the voltage Vc (arbitrarily, we considered 1% here) and the estimated current (see (1)).

$$C = \frac{I \times \Delta t}{\Delta V} \tag{1}$$

where:

- I is the estimated current;
- ΔV is the ripple of the voltage Vc, which is constant (i.e., 1%);
- $\Delta t = \alpha T = \frac{\alpha}{F}$ with α as the duty cycle and F as the switching frequency.

2.3. Control Strategies

In this section of the paper, we will describe the control strategies of the proposed bidirectional DC–AC converter. We will only give the principles and thus, we will not detail the control circuit or the AC network connection strategy because several patents are pending.

2.3.1. Inverter Mode

In inverter mode (see Figure 3), energy flowed from the storage system to the AC grid. In this type of operation, the most important objective was to control the current injected into the AC grid by regulating the output voltage of the DC–DC stage. Figure 6 shows the overall architecture of the MOSFET control circuit inside the DC–DC stage (see transistors $T1$ and $T2$ in Figure 2). We recall that this stage supervised the generation of a semi-sinusoidal output signal. The possibility of modifying the injected current was the indispensable aspect of this control strategy. Figure 6 shows that the microcontroller was programmed to adjust the duty cycle from zero to one with great precision.

A minor increase or decrease in this variable caused the current injected into the AC grid to increase or decrease. This allowed us to control the selection of the operating mode and provided us with the ability to switch from inverter to rectifier mode, as we will see later.

The DC–AC stage, on the other hand, was controlled using the frequency measurement of the smart meter with a switching frequency of 50 Hz in order to be synchronized with the grid (see transistors from $T3$ to $T6$ in Figure 2).

2.3.2. PFC Rectifier Mode

In PFC rectifier mode (see Figure 4), energy flowed from the AC grid to the storage system. In this kind of operation, the most important objective was to control the absorbed current, which needed a sinusoidal waveform. This objective could be achieved by adjusting the equivalent capacitance of the modulation stage of the DC–DC stage (see Case 3 in Figure 5). As for the inverter mode, we chose the solution with a capacitance $C2$ equal to 1 µF because it offered the best results. The PFC mode, achieved by the DC–DC stage, was essential to meet the requirements of IEC 61000-3-2.

Figure 7 shows the structure of the control circuit of the MOSFETs inside the DC–DC stage. The regulation of the control circuit was made possible by a current sensor and a voltage sensor to realize the PFC strategy.

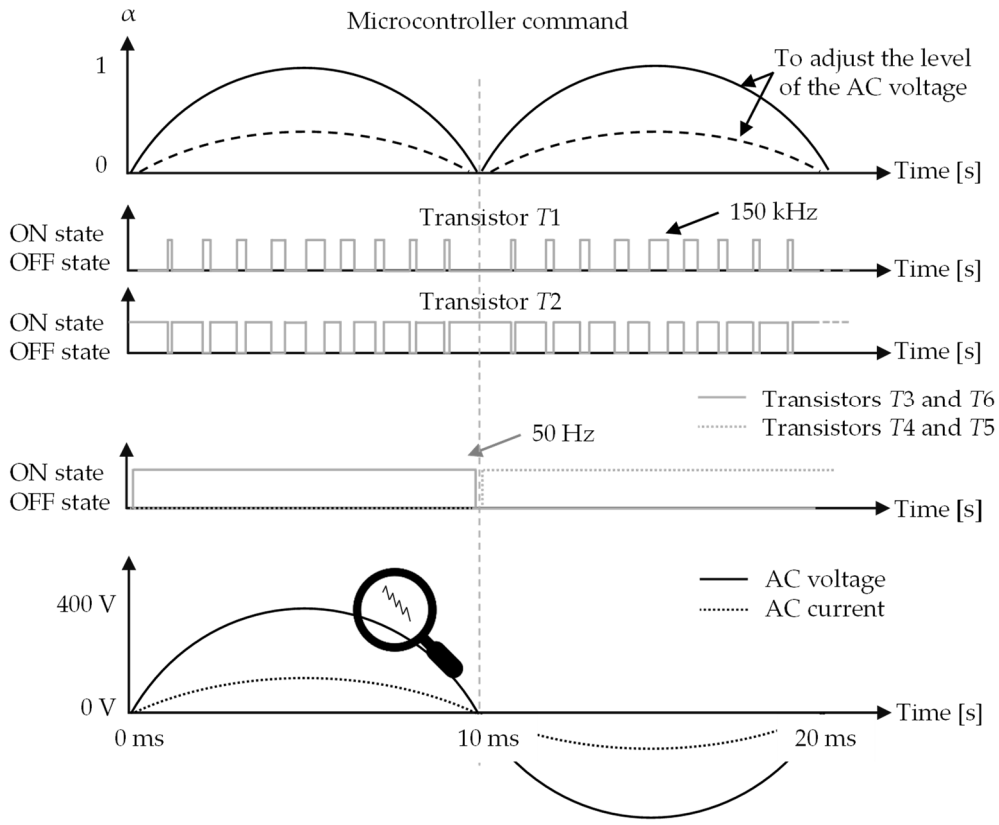

Figure 6. Control strategy of the MOSFETs inside the proposed bidirectional DC–AC converter used in inverter mode.

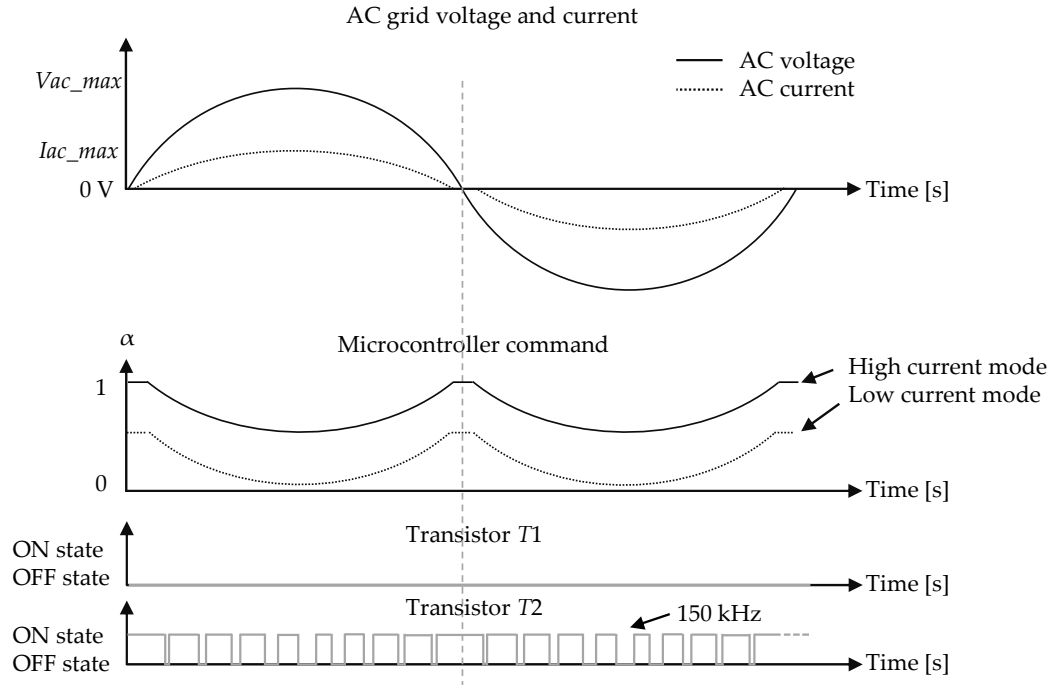

Figure 7. Control strategy of the MOSFETs inside the proposed bidirectional DC–AC converter used in PFC rectifier mode.

The DC–AC stage was controlled by the very same signal as the inverter mode, so it was synchronized with the AC grid at a switching frequency of 50 Hz.

3. Sizing of the Bidirectional Converter and Main Results in Grid-Connected Mode

3.1. Specifications, Key Sizing Steps and Selection of the Main Components

The specifications of the prototype bidirectional DC–AC converter that we realized are listed in Table 1. The electrical waveforms were evaluated based on the topology and control strategies detailed in the previous section.

Table 1. The specifications of the proposed bidirectional DC–AC converter.

	Parameters	Values
AC bus	RMS voltage (V)	110/230
	Frequency (Hz)	50/60
	Grid capacitor (µF) (see C_{AC} in Figure 2)	1
DC bus	DC voltage (V)	400
DC–DC stage	Input current (A)	10 max.
	Output current (A)	5 max.
	Switching frequency (kHz)	150/300
DC–AC stage	Output current (A)	5 max.
	Switching frequency (Hz)	AC grid frequency
Targeted power		From 100 W up to 1.5 kW
Targeted efficiency		About 95% over the entire power range considered

The approach to the sizing of the converter was classical because the two stages taken separately are now well-known and mastered [36–40]. Of course, this approach is adaptable according to the targeted application and design constraints. Figure 8 presents the key steps for the sizing of the passive and active components of each of the two stages. In this approach, the following parameters were essential to take into account:

- The static and dynamic losses in the MOSFETs (in the DC–DC stage, which switched at several hundred kilohertz, it was particularly important to determine the switching losses) and the losses in the passive components (it was particularly important to take into account the losses in the core of the DC–DC stage choke due to hysteresis and eddy currents) to reach the efficiency objectives;
- The thermal management of the components over the targeted power range;
- The choice of the technology and the packaging of the components to optimize the compactness and mass of the converter;
- Other constraints in view of the industrialization of the product, such as electromagnetic compatibility problems and also the development cost.

As shown in Figure 8, the main components to be sized were the power MOSFETs of both stages [36–38], the inductor of the DC–DC stage [39,40] and the output voltage modulation of the DC–DC stage [26].

For the power MOSFETs, given the high switching frequency of the DC–DC stage (a few hundred kilohertz) and to optimize the thermal management of the components, we chose silicon carbide (SiC) devices. For the DC–AC stage, which switched at the AC grid frequency, silicon substrate components were perfectly suited. Then, whatever the two stages, it was essential to take into account: the voltage withstand; the current flowing in the drain; the switching characteristics, especially the rise and fall times for the components of the DC–DC stage; the gate charge characteristics; the characteristics of the body diodes; and the thermal characteristics, in terms of junction temperature and thermal resistances.

The choice of power MOSFETs also took into account future normative tests, which are essential before the industrialization of the product, such as immunity to burst transients, resistance to electrostatic discharges and electromagnetic compatibility. As shown in Figure 9 and Table 2, the DC–DC stage used two (see *T*1 and *T*2 in Figure 9) SiC MOSFETs (reference: SCT3080AL; manufacturer: ROHM semiconductor) with, for these two transistors, a nominal drain current and drain-to-source voltage equal to 30 A and 650 V, respectively. Two switching frequencies were considered: 150 kHz and 300 kHz. Switching

the components of this stage at 300 kHz allowed for the drastic reduction in the size of the passive components and a fortiori the optimization of the size of the converter. On the other hand, this penalized the efficiency of the system (the desired efficiency of 95% was difficult to achieve) because the switching losses were very significant (see Section 4.2). Therefore, the switching frequency of 150 kHz was implemented experimentally in order to obtain a compromise between the compactness of the system, its efficiency over the entire power range (i.e., from 100 W to 1.5 kW) and the optimization of its power quality; this last point will be studied in more detail in the near future. As for the DC–AC stage, as shown in Table 2 and Figure 9, it used four MOSFETs (designated *T*3, *T*4, *T*5 and *T*6) on a silicon substrate (reference: IRFPS43N50K; manufacturer: Vishay Siliconix), each with a nominal drain current and drain-to-source voltage equal to 47 A and 500 V, respectively. The power devices were turned on and off with zero crossing of the AC grid voltage to minimize losses.

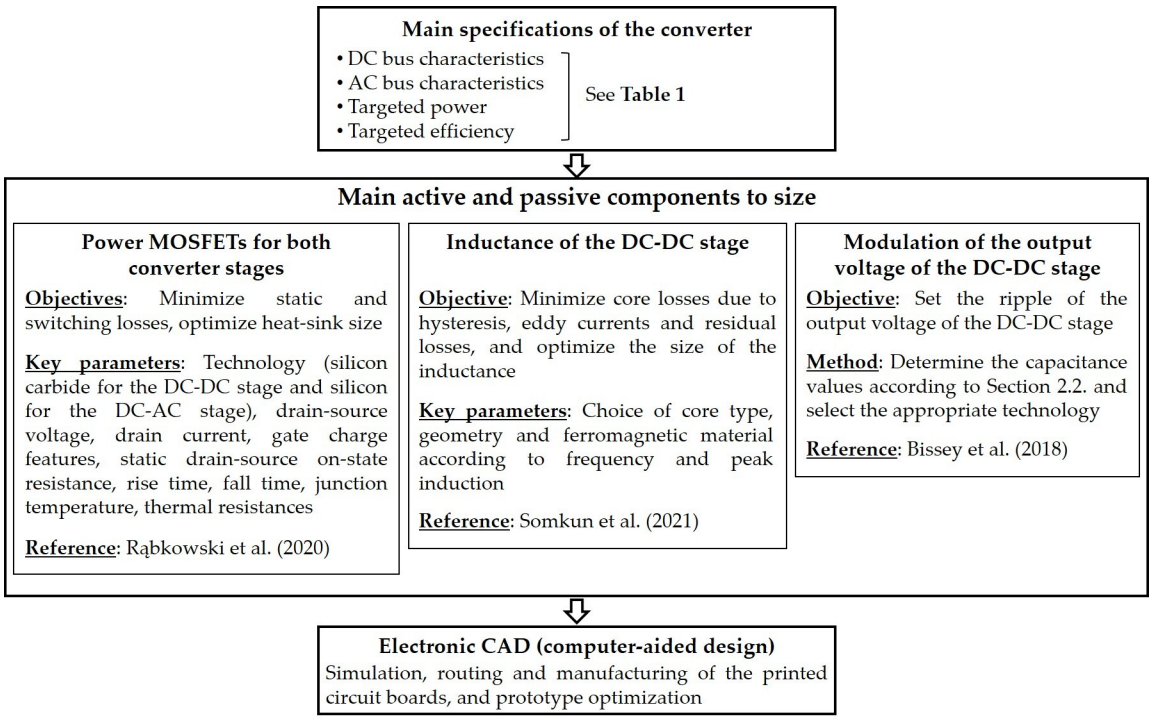

Figure 8. The key sizing steps of the proposed converter [26,38,40].

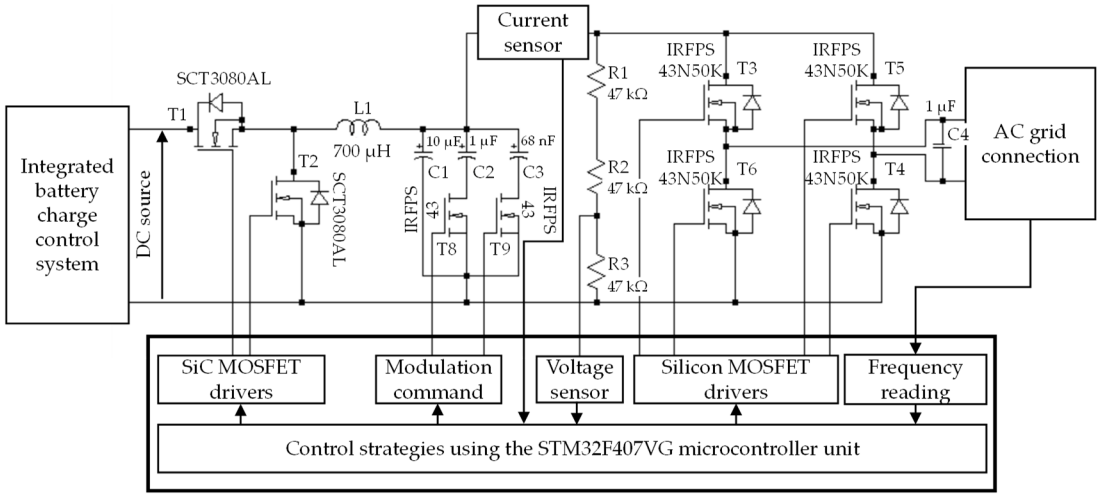

Figure 9. Electrical diagram of the power circuit of the converter.

Table 2. A selection of the main components.

Parameters		Values
DC–DC stage	Inductance of the DC coil (µH) (see *L*1 in Figure 9)	700
	Power MOSFETs used (see *T*1 and *T*2 in Figure 9)	Two N-channel SiC power MOSFETs of 650 V, 30 A, 80 mΩ (part number: SCT3080AL; manufacturer: ROHM Semiconductor); switching frequency of a few hundred kHz (150 kHz implemented experimentally)
Modulation stage	Capacitances (µF) (see *C*1, *C*2 and *C*3 in Figure 9)	10 (*C*1), 1 (*C*2) and 0.068 (*C*3)
	Power MOSFETs used (see *T*8 and *T*9 in Figure 9)	Two N-channel power MOSFETs of 500 V, 47 A, 78 mΩ (part number: IRFPS43N50K; manufacturer: Vishay Siliconix).
DC–AC stage	Power MOSFETs used (see *T*3, *T*4, *T*5 and *T*6 in Figure 9)	Four N-channel power MOSFETs of 500 V, 47 A, 78 mΩ (part number: IRFPS43N50K; manufacturer: Vishay Siliconix); switching to AC mains frequency (50 Hz here)
Control strategies (SiC and silicon MOSFET drivers, voltage/current sensors, AC grid frequency reading)		Microcontroller based on the Arm® Cortex®-M4 32-bit RISC (reduced instruction set computer) core, operating at a frequency of up to 168 MHz (part number: STM32F407VG; manufacturer: STMicroelectronics)

Concerning the optimization of the DC–DC stage inductance in terms of electromagnetic characteristics, compactness and mass, we took into account the geometry, toroidal or planar and the type of core, as well as the ferromagnetic material used, according to the frequency and the maximum induction [39,40]. Several technologies were studied in order to determine the most suitable inductance for the sized converter. The choice of the 700 µH inductor (see *L*1 in Figure 9) was based on limiting the current ripple in the inductor to less than 20% of the maximum current (i.e., 5 A here) [41]. We also considered its maximum DC resistance (0.12 Ω) and the evolution of its impedance with frequency. Considering all these elements, we chose the WE-FI leaded toroidal line choke from the manufacturer Wurth Electronik.

Regarding the output voltage modulation of the DC–DC stage, the value of the capacitors (see *C*1, *C*2 and *C*3 in Figure 9) was explained in Section 2.2.

Concerning the servo strategy of the proposed converter, a differential measurement was used to determine the AC bus voltage as a function of the phase potential (*VL*) and the neutral point potential (*VN*). This differential measurement was performed with a voltage divider bridge of the same resistance value, i.e., 47 kΩ (see *R*1, *R*2 and *R*3 in Figure 9). To measure the current flowing between the DC–DC stage and the DC–AC stage, as shown in Figure 9, a 15 A closed-loop Hall transducer (reference: LKSR 15-NP; manufacturer: LEM) was used in series with the inductor of the DC–DC stage.

Finally, an STM32F407VG microcontroller unit from the manufacturer STMicroelectronics drove the entire converter and provided automatic AC grid connection and disconnection. The control board with the microcontroller, the MOSFET drivers and the control strategies of the power components are currently under patent and cannot be detailed in this manuscript.

3.2. Experimental Test Setup and Standby Mode

A comprehensive experimental process was adopted to validate the two modes of operation of the bidirectional DC–AC converter proposed here when connected to the AC grid and in a power range up to 1.5 kW. The converter demonstrator naturally included the DC–DC and DC–AC stages, but also an adaptive filter, as well as a power supply (i.e., +5 V and +12 V) to power the onboard electronics.

As shown in Figure 10, four 12 V, 7 Ah batteries (reference: NP7-12; manufacturer: YUASA) were used to simulate the storage system. These batteries were associated in series to provide the overall voltage of 48 V (see ❶ in Figure 10). On the AC side, the connection to the power supply was provided by a single-pole variable transformer (reference: SEC2; manufacturer: LANGLOIS) set at 110 V RMS. A line impedance stabilization network (LISN) (reference: PD30; manufacturer: EMC MASTER; main features: monophasic, 220 V, 10 A, 150 kHz to 30 MHz) was used to control the network impedance and ensure measurement repeatability (see ❷ in Figure 10).

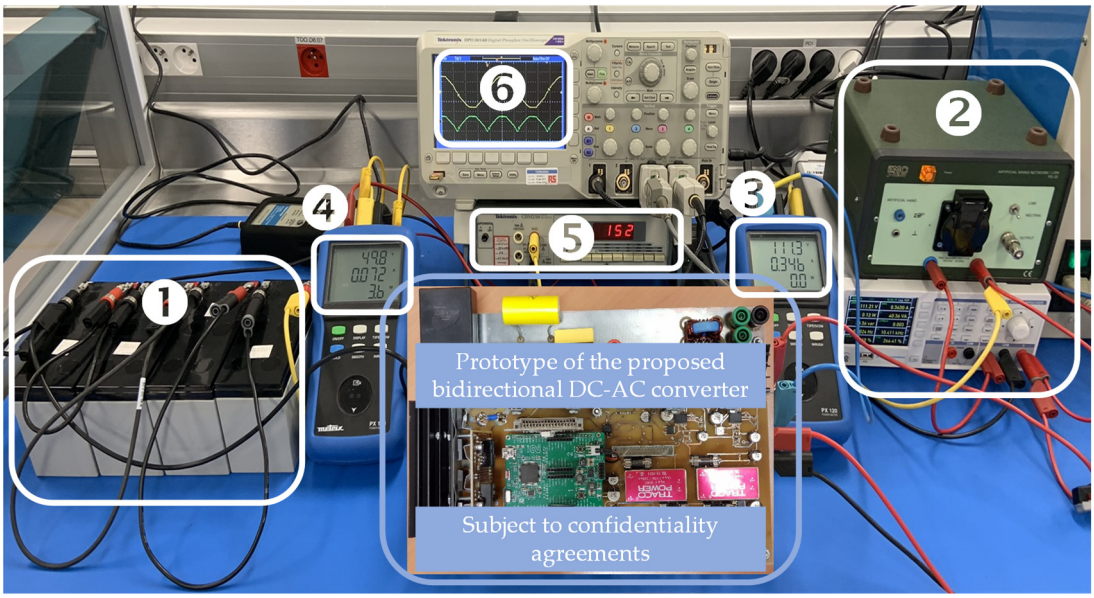

Figure 10. The experimental test setup.

A high-voltage differential probe (reference: P5205; manufacturer: Tektronix) and a 15 A AC–DC current probe (reference: TCP202; manufacturer: Tektronix) were used to measure the output voltage and current, respectively. The output power of the DC–DC stage was measured using a power meter (reference: PX 110; manufacturer: Metrix). For the measurement of the output power of the DC–AC stage, the same type of electronic meter was used.

To connect to the AC grid, the bidirectional DC–AC converter used a patent-pending automated routine. Figure 10 shows the converter in a steady state with the grid at 0 watts (see ❸ in Figure 10) and the batteries powering the system. The power consumption of the converter in sleep mode was 3.6 W (see ❹ in Figure 10). The DC bus was monitored (see ❺ in Figure 10) and displayed the DC voltage (see ❸ in Figure 2), while differential probes were used to monitor the voltage generated between the two stages of the converter, as well as that between the converter and the grid connection (see ❻ in Figure 10, as well as Figure 11).

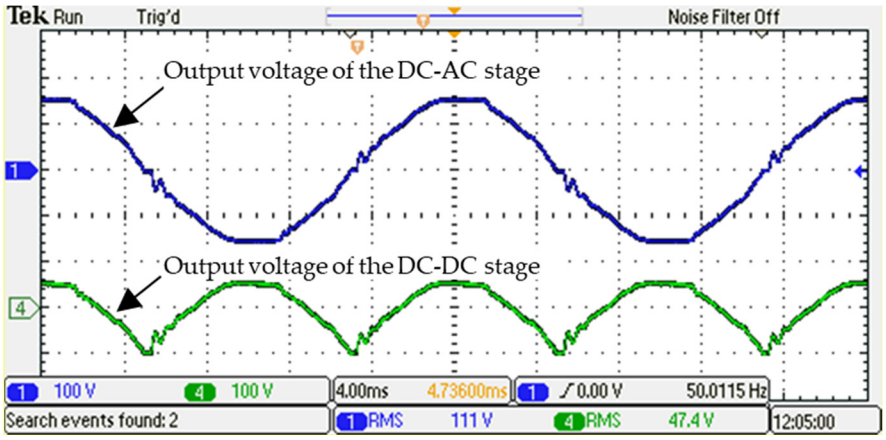

Figure 11. Experimental validation of the standby mode: output signals.

3.3. Experimental Validation of the Operating Modes

3.3.1. Foreword

This section of the paper aims to validate the two operation modes (i.e., inverter and PFC rectifier) of the proposed bidirectional DC–AC converter. To avoid damage to the prototype of the whole converter, the experimental tests were performed at low power. The

single-pole variable transformer was used to adjust the grid voltage to 110 V RMS, 50 Hz, while the DC side was connected to the four Yuasa batteries for a total of 48 volts DC. The prototype also included a charge–discharge management system, capable of supplying up to 350 V DC to the whole converter.

The RMS voltage and frequency were monitored by the microcontroller on both sides of the primary switch connecting the converter to the AC grid (see Figure 2). The switch was closed when all criteria for grid connection were met [36], and the voltage on both sides of the converter was balanced using the duty cycle adjustable by the control circuit. Therefore, the bidirectional converter could operate in inverter or PFC rectifier mode, depending on the state of the AC grid. Thus, the HEMS provided a corresponding signal that forced the bidirectional converter to inject electricity into the grid (inverter mode) or to charge the batteries (PFC rectifier mode). Two buttons were added to the microcontroller to substitute the HEMS signal for the following results. The duty cycle could be adjusted, and the power direction and operating mode could be controlled with these two buttons.

Between the batteries and the DC–DC stage, a third stage was introduced for this experiment. The purpose of this stage was to modify the charge and the injection of electricity and to adapt the voltage and the current between the DC–DC stage and the batteries.

The following two subsections examine these two modes of operation in detail.

3.3.2. Inverter Mode

The objective here was to confirm the proper operation of the bidirectional DC–AC converter in inverter mode. Figure 12 shows an example of the experimental results in this mode, where the batteries supplied 485 W to the whole system. In this example, the DC bus voltage was 178 V; this voltage represented the input DC voltage of the bidirectional converter. Figure 12 shows the output voltage of the DC–DC stage, confirming the sine half-wave, here at the RMS voltage of 126 V (measured using ❺ in Figure 10). The output of the DC–AC stage was a 50 Hz sine wave with, here, an RMS voltage of 120 V. This signal was applied to the AC grid and the power was effectively negative in this case (measured using ❸ in Figure 10) since power was being injected (in this example, 410 W). Figure 12 also shows the current injected into the AC grid, here with an RMS value of 2 A. As the current was imposed by the converter, it was necessarily out-of-phase with the voltage. While the inverter was injecting power into the AC grid, the voltage would remain constant even if the current changed.

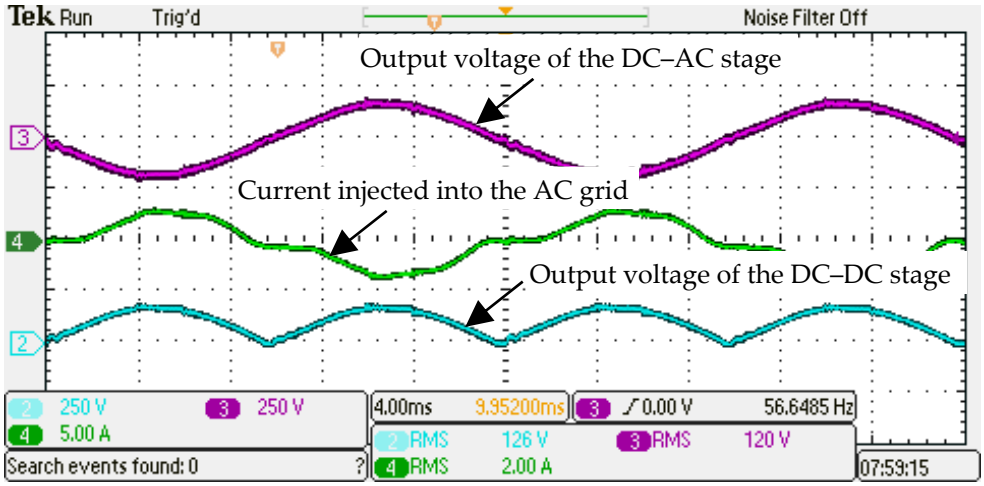

Figure 12. Experimental validation of the inverter mode: output signals.

3.3.3. PFC Mode

The objective here was to confirm the proper operation of the bidirectional DC–AC converter in PFC rectifier mode. First, it was essential to demonstrate that the power factor

modification was indeed feasible in this case. The sinusoidal current could be absorbed by appropriately controlling transistor *T*2 of the DC–DC stage (see Figure 9).

Figure 13 shows an example of the experimental results in PFC mode. In this configuration, the AC grid delivered a positive power of 80 W to the whole system (measured using ❸ in Figure 10). The power transmitted to the batteries via the bidirectional converter was necessarily negative in this case, which indicates that we were in a charge cycle (indicated by ❹ in Figure 10). Figure 13 shows the sine wave imposed by the AC grid, as well as the half-sine curve between the DC–DC stage and the DC–AC stage, while we monitored the input of the DC–AC stage. Figure 13 shows an RMS voltage of the half-sine wave of 49 V, while the voltage at the DC bus was 166 V (measured using ❺ in Figure 10).

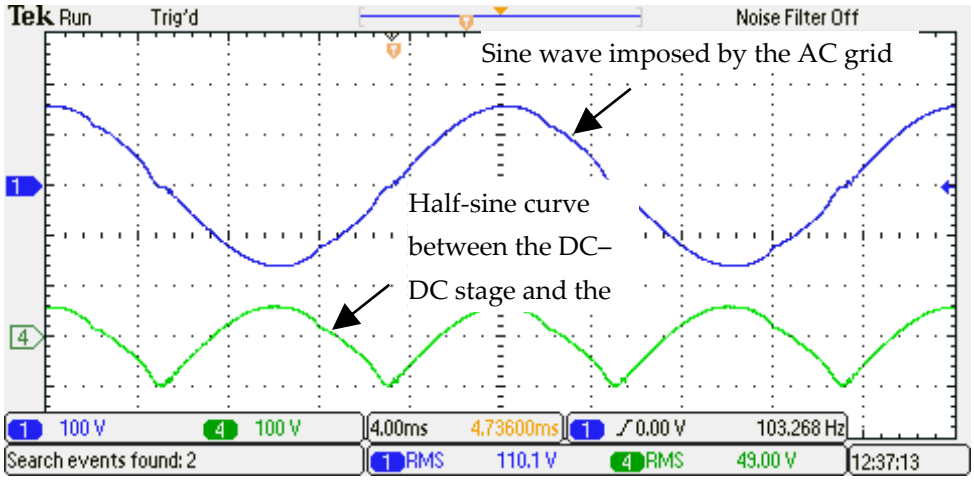

Figure 13. Experimental validation of the PFC mode: output signals.

In this example, the voltage and the absorbed current were imposed in order to follow the charge curve of the batteries.

4. Discussion

4.1. Switching of the HEMS Control

The main objective of this work was to design and implement a bidirectional DC–AC converter that was connected to an HEMS system [23]. The HEMS system supervised the control of several elements of the converter, such as:

- Automatically connecting the converter to the AC grid in standby mode, which ensured a balanced condition between the energy supplied by the batteries and the electricity supplied by the AC grid (see Figures 9 and 10);
- Inverter mode: In this mode, the HEMS determined the amount of energy to be supplied to the grid by changing the duty cycle of the control signals. This allowed us to provide the precise amount of energy required. In the example described in Figure 12, we changed the duty cycle to inject 410 W; depending on the state of the grid, this amount could be as much as 1.5 kW;
- PFC rectifier mode: In this mode, the system operated as a battery management system (BMS). The HEMS could read the state of charge (SoC) of the batteries and adjust the voltage and current sent to the batteries in order to store the precise amount of excess energy available from the AC grid (see Figure 13).

At this stage, the bidirectional DC–AC converter was tested on a 110 V, 50 Hz AC grid. The next experiments will be performed on a 230 V, 50 Hz AC grid. The converter is fully self-adaptive and, therefore, requires no human interaction; all of the above parameters can be modified using real-time data measurements provided by the HEMS.

The experimentally designed and implemented bidirectional DC–AC converter is compatible with the HEMS system that we recently developed in [23]. Therefore, it can be

fully used either to store excess energy available on the AC grid in batteries or to inject energy into the AC grid, according to the consumption patterns defined in the house.

4.2. Efficiency of the Whole Converter

This section of the manuscript aims to study in detail the efficiency of the proposed bidirectional DC–AC converter and, more specifically, when it operates in inverter mode. The PFC rectifier mode was regulated by the battery management system and thus, depended on the battery state of charge. The amount of energy stored could be varied but was comparable to the voltage and current measurements in the batteries, as well as the charge curves of the storage system. Combined with the charge control system, the overall efficiency of the system shown in the example in Figure 13 was approximately 85%.

In grid-connected inverter mode, we performed the efficiency measurements at low power (a few tens of watts) and up to 1.5 kW. The measurements were tricky to perform because we needed to ensure that the power injected by the batteries was flowing through the charge–discharge management system and that the power was detected at the output using the DC voltage and current measurements shown in Figure 12.

Figure 14 shows the evolution of the efficiency of the bidirectional DC–AC converter as a function of the rated output power. Figure 14 shows that the average efficiency of the whole converter was about 96.5%, from 100 W to 1.5 kW. It should be noted that it would be difficult to achieve any better given the general architecture chosen, i.e., the series connection of a DC–DC stage and a DC–AC stage, even if the DC–DC stage presented excellent performances (average efficiency of 98.5% over the tested power range). At very low power (e.g., 50 W), although the 95% target was not reached, the values obtained (here about 91.5% at 50 W) were more than satisfactory compared to other topologies discussed in the literature.

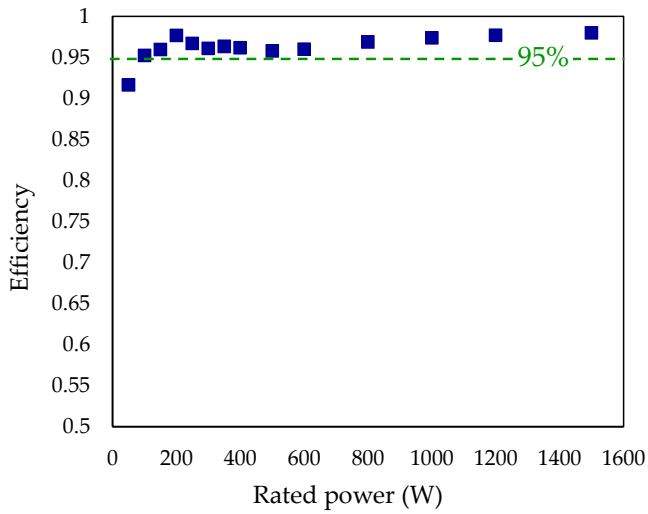

Figure 14. The efficiency of the bidirectional DC–AC converter in inverter mode (experimental results).

The losses were distributed mainly by the MOSFETs and the passive devices, especially the inductance of the DC–DC stage. The classical ferrite core was banned from this prototype because it caused too many losses in the iron. Therefore, we chose a high flux core that was ideal for high frequencies. To be more precise, the losses in the MOSFETs represented 1.1% of the target power, while the losses in the DC–DC stage inductor represented 2.4% of the target power. Conduction losses and switching losses could be estimated from the key characteristics (including drain-to-source on-state resistance, rise time and fall time) of each MOSFET. These losses represented 0.1% and 1% of the target power, respectively. By adjusting the reference of the SiC devices used in the DC–DC stage, for example with 36 A, 900 V SiC MOSFETs from the manufacturer Cree, it was possible to reduce the losses of the MOSFETs and gain nearly 0.5 percentage points in efficiency.

Compared to the first converter presented in [26] (this converter was experimentally tested in islanding mode), we intentionally decreased the switching frequency of the MOSFETs in the DC–DC stage from 300 kHz to 150 kHz. At 300 kHz, the converter efficiency lost, on average, 0.3 efficiency points over the output power range studied here. By switching to 150 kHz, we optimized the efficiency and, in addition, anticipated future electromagnetic compatibility issues, which we will detail in the near future.

5. Conclusions

In this paper, the main objective was to present and experimentally validate a bidirectional DC–AC converter, connected to the AC grid and suitable for HEMS applications when an energy storage system is required. The proposed topology was based on two necessarily bidirectional stages associated in series: the first being a DC–DC stage composed of two silicon carbide power MOSFETs, which were controlled at high frequency (the frequency of 150 kHz was implemented experimentally); the second being an H-bridge composed of four MOSFETs on silicon substrate, which were controlled at the frequency of the AC grid (i.e., 50 Hz here). With this converter architecture, the DC–DC stage regulated the DC voltage and established the positive parts of an AC waveform, while the DC–AC stage reversed it to obtain the sinusoidal voltage. Thus, the proposed structure provided an excellent AC waveform, but the latter depended mainly on the DC–DC stage.

A complete experimental procedure was defined and implemented to validate the operating modes of the bidirectional DC–AC converter, i.e., the inverter mode and the PFC rectifier mode, especially in the case of a grid connection. The energy efficiency of the whole DC–AC converter operating in inverter mode was evaluated and exceeded the target of 95% over the entire power range studied, i.e., from 100 W to 1.5 kW.

The three main outcomes of this study are summarized below:

1. The complexity of the topology is reasonable, so it can be recommended as an alternative solution for HEMS applications;
2. In the case of stand-alone inverter operation and unlike traditional H-bridges, the proposed converter does not require the use of a bulky filter, which optimizes its compactness. The optimization of the compactness of the whole system is made possible by the use of silicon carbide MOSFETs in the DC–DC stage, switching at several hundred kilohertz (the frequencies of 150 kHz and 300 kHz were investigated here and the 150 kHz frequency was implemented experimentally);
3. The proposed bidirectional DC–AC converter can operate in a grid-connected configuration, with the ability to charge batteries during off-peak hours and use the energy from those batteries during peak loads. The operating mode of the entire converter is controlled by the previously presented HEMS system [23].

The experimental results demonstrate the expected performance of such a system, both in terms of its operating modes and its high energy efficiency. The bidirectional switching of the components of this architecture is autonomous in adjusting the control commands of the microcontroller, as well as controlling the amount of energy to store or inject into the grid. The algorithm of the control strategy, the communication between the developed system and the smart meter are being patented.

The short-term perspectives of this work are as follows. The bidirectional DC–AC converter was developed to operate in both grid and off-grid mode. The islanding mode will be presented in another paper. In addition, the electromagnetic compatibility aspects will have to be realized in order to conform with the standards of connection to the AC grid that are in application. In the longer term, the whole converter and the HEMS will be installed in real smart homes and the profitability of our approach will be evaluated.

Author Contributions: Conceptualization, J.-C.L.B. and S.B.; methodology, J.-C.L.B., S.J., S.B. and I.A.; software, S.B., C.R., I.A. and T.B.; validation, I.A., T.B. and J.-C.L.B.; formal analysis, J.-C.L.B. and S.B.; investigation, S.B., C.R., I.A., T.B. and J.-C.L.B.; resources, J.-C.L.B.; data curation, , I.A., S.J. and J.-C.L.B.; writing—original draft preparation, S.B. and S.J.; writing—review and editing, I.A., S.J. and

J.-C.L.B.; visualization, I.A., S.J. and J.-C.L.B.; supervision, J.-C.L.B.; project administration, S.J. and J.-C.L.B.; funding acquisition, S.J. and J.-C.L.B. All authors have read and agreed to the published version of the manuscript.

Funding: These research activities were supported by "Région Centre Val-de-Loire" (research project number: 2015-00099656). The authors of this paper thank our colleagues from this institution who provided insight and expertise that greatly assisted the project.

Institutional Review Board Statement: Not applicable.

Informed Consent Statement: Not applicable.

Conflicts of Interest: The authors declare to respect the confidentiality clauses currently defined in the collaboration contract defined above.

Abbreviations

The following abbreviations are used in this paper:

AC	Alternating current
AI	Artificial intelligence
ANFIS	Adaptive neural fuzzy inference systems
ANN	Artificial neural networks
BMS	Battery management system
CAD	Computer-aided design
DC	Direct current
DL	Deep learning
FLC	Fuzzy logic control
GA	Genetic algorithms
HEMS	Home electricity management systems
IoT	Internet of things
MOSFET	Metal oxide semiconductor field effect transistor
MPC	Model predictive control
PSO	Particle swarm optimization
PFC	Power factor correction
PV	Photovoltaics
PWM	Pulse width modulation
RISC	Reduced instruction set computer
RMS	Root mean square
RNN	Recurrent neural networks
SiC	Silicon carbide
SoC	State of charge
THD	Total harmonic distortion
Triac	Triode for alternating current
VSC	Voltage–source converter

References

1. Javaid, N.; Javaid, S.; Abdul, W.; Ahmed, I.; Almogren, A.; Alamri, A.; Niaz, I.A. A Hybrid Genetic Wind Driven Heuristic Optimization Algorithm for Demand Side Management in Smart Grid. *Energies* **2017**, *10*, 319. [CrossRef]
2. Torriti, J. The Risk of Residential Peak Electricity Demand: A Comparison of Five European Countries. *Energies* **2017**, *10*, 385. [CrossRef]
3. Kornatka, M.; Gawlak, A. An Analysis of the Operation of Distribution Networks Using Kernel Density Estimators. *Energies* **2021**, *14*, 6984. [CrossRef]
4. Elfeki, I.; Jacques, S.; Aouichak, I.; Doligez, T.; Raingeaud, Y.; Le Bunetel, J.-C. Characterization of Narrowband Noise and Channel Capacity for Powerline Communication in France. *Energies* **2018**, *11*, 3022. [CrossRef]
5. Markkula, J.; Haapola, J. Shared LTE Network Performance on Smart Grid and Typical Traffic Schemes. *IEEE Access* **2020**, *8*, 39793–39808. [CrossRef]
6. Lu, H.H.-C.; Chu, C.-C.; Nwankpa, C.O.; Wu, C.W. Guest Editorial Complex Network for Modern Smart Grid Application—Part 2: Stability, Reliability and Resilience Issues. *IEEE J. Emerg. Sel. Top. Circuits Syst.* **2017**, *7*, 345–348.
7. Iqbal, Z.; Javaid, N.; Iqbal, S.; Aslam, S.; Ali Khan, Z.; Abdul, W.; Almogren, A.; Alamri, A. A Domestic Microgrid with Optimized Home Energy Management System. *Energies* **2018**, *11*, 1002. [CrossRef]

8. Kim, Y.-S.; Hwang, C.-S.; Kim, E.-S.; Cho, C. State of Charge-Based Active Power Sharing Method in a Standalone Microgrid with High Penetration Level of Renewable Energy Sources. *Energies* **2016**, *9*, 480. [CrossRef]
9. Khan, S.; Khan, R. Elgamal Elliptic Curve Based Secure Communication Architecture for Microgrids. *Energies* **2018**, *11*, 759. [CrossRef]
10. Jelić, M.; Batić, M.; Tomašević, N. Demand-Side Flexibility Impact on Prosumer Energy System Planning. *Energies* **2021**, *14*, 7076. [CrossRef]
11. Dinh, H.T.; Yun, J.; Kim, D.M.; Lee, K.; Kim, D. A Home Energy Management System with Renewable Energy and Energy Storage Utilizing Main Grid and Electricity Selling. *IEEE Access* **2020**, *8*, 49436–49450. [CrossRef]
12. Floris, A.; Porcu, S.; Girau, R.; Atzori, L. An IoT-Based Smart Building Solution for Indoor Environment Management and Occupants Prediction. *Energies* **2021**, *14*, 2959. [CrossRef]
13. Pavón, R.M.; Alberti, M.G.; Álvarez, A.A.A.; del Rosario Chiyón Carrasco, I. Use of BIM-FM to Transform Large Conventional Public Buildings into Efficient and Smart Sustainable Buildings. *Energies* **2021**, *14*, 3127. [CrossRef]
14. Leitão, J.; Gil, P.; Ribeiro, B.; Cardoso, A. A Survey on Home Energy Management. *IEEE Access* **2020**, *8*, 5699–5722. [CrossRef]
15. Mariano-Hernández, D.; Hernández-Callejo, L.; Zorita-Lamadrid, A.; Duque-Pérez, O.; Santos García, F. A review of strategies for building energy management system: Model predictive control, demand side management, optimization, and fault detect & diagnosis. *J. Build. Eng.* **2021**, *33*, 101692.
16. Atef, S.; Ismail, N.; Eltawil, A.B. A New Fuzzy Logic Based Approach for Optimal Household Appliance Scheduling Based on Electricity Price and Load Consumption Prediction. In *Advances in Building Energy Research*; Taylor & Francis, 2021; pp. 1–19. Available online: https://cogentoa.tandfonline.com/doi/abs/10.1080/17512549.2021.1873183?journalCode=taer20 (accessed on 21 December 2021).
17. Bot, K.; Santos, S.; Laouali, I.; Ruano, A.; Ruano, M.d.G. Design of Ensemble Forecasting Models for Home Energy Management Systems. *Energies* **2021**, *14*, 7664. [CrossRef]
18. Andriopoulos, N.; Magklaras, A.; Birbas, A.; Papalexopoulos, A.; Valouxis, C.; Daskalaki, S.; Birbas, M.; Housos, E.; Papaioannou, G.P. Short Term Electric Load Forecasting Based on Data Transformation and Statistical Machine Learning. *Appl. Sci.* **2021**, *11*, 158. [CrossRef]
19. Franco, P.; Martínez, J.M.; Kim, Y.-C.; Ahmed, M.A. IoT Based Approach for Load Monitoring and Activity Recognition in Smart Homes. *IEEE Access* **2021**, *9*, 45325–45339. [CrossRef]
20. Hosseinnezhad, V.; Shafie-Khah, M.; Siano, P.; Catalão, J.P.S. An Optimal Home Energy Management Paradigm with an Adaptive Neuro-Fuzzy Regulation. *IEEE Access* **2020**, *8*, 19614–19628. [CrossRef]
21. Zupančič, J.; Filipič, B.; Gams, M. Genetic-programming-based multi-objective optimization of strategies for home energy-management systems. *Energy* **2020**, *203*, 117769. [CrossRef]
22. Yousefi, M.; Hajizadeh, A.; Soltani, M.N.; Hredzak, B. Predictive Home Energy Management System with Photovoltaic Array, Heat Pump, and Plug-In Electric Vehicle. *IEEE Trans. Ind. Inform.* **2021**, *17*, 430–440. [CrossRef]
23. Bissey, S.; Jacques, S.; Le Bunetel, J.-C. The Fuzzy Logic Method to Efficiently Optimize Electricity Consumption in Individual Housing. *Energies* **2017**, *10*, 1701. [CrossRef]
24. Khan, M.; Seo, J.; Kim, D. Towards Energy Efficient Home Automation: A Deep Learning Approach. *Sensors* **2020**, *20*, 7187. [CrossRef] [PubMed]
25. Bhatt, D.; Hariharasudan, A.; Lis, M.; Grabowska, M. Forecasting of Energy Demands for Smart Home Applications. *Energies* **2021**, *14*, 1045. [CrossRef]
26. Bissey, S.; Jacques, S.; Reymond, C.; Le Bunetel, J. An Innovative Bidirectional DC-AC Converter to Improve Power Quality in a Grid-Connected Microgrid. *Preprints* **2018**, 2018070252. [CrossRef]
27. Ali Khan, M.Y.; Liu, H.; Yang, Z.; Yuan, X. A Comprehensive Review on Grid Connected Photovoltaic Inverters, Their Modulation Techniques, and Control Strategies. *Energies* **2020**, *13*, 4185. [CrossRef]
28. Bughneda, A.; Salem, M.; Richelli, A.; Ishak, D.; Alatai, S. Review of Multilevel Inverters for PV Energy System Applications. *Energies* **2021**, *14*, 1585. [CrossRef]
29. Alotaibi, S.; Darwish, A. Modular Multilevel Converters for Large-Scale Grid-Connected Photovoltaic Systems: A Review. *Energies* **2021**, *14*, 6213. [CrossRef]
30. Martinez-Rodrigo, F.; Ramirez, D.; Rey-Boue, A.B.; De Pablo, S.; Herrero-de Lucas, L.C. Modular Multilevel Converters: Control and Applications. *Energies* **2017**, *10*, 1709. [CrossRef]
31. Lourenço, L.F.N.; Perez, F.; Iovine, A.; Damm, G.; Monaro, R.M.; Salles, M.B.C. Stability Analysis of Grid-Forming MMC-HVDC Transmission Connected to Legacy Power Systems. *Energies* **2021**, *14*, 8017. [CrossRef]
32. Jacques, S.; Reymond, C.; Le Bunetel, J.-C.; Benabdelaziz, G. Comparison of the power balance in a Totem-Pole Bridgeless PFC topology with several inrush current limiting strategies. *J. Electr. Eng.* **2021**, *72*, 12–19. [CrossRef]
33. Amiri, P.; Eberle, W.; Gautam, D.; Botting, C. An Adaptive Method for DC Current Reduction in Totem Pole Power Factor Correction Converters. *IEEE Trans. Power Electron.* **2021**, *36*, 11900–11909. [CrossRef]
34. Yang, Z. Bidirectional DC-to-AC inverter with improved performance. *IEEE Trans. Aerosp. Electron. Syst.* **1999**, *35*, 533–542. [CrossRef]
35. Koutroulis, E.; Chatzakis, J.; Kalaitzakis, K.; Voulgaris, N.C. A bidirectional, sinusoidal, high-frequency inverter design. *IEE Proc. Electr. Power Appl.* **2001**, *148*, 315. [CrossRef]

36. Zhang, J.; Shao, J.; Xu, P.; Lee, F.C.; Jovanovic, M.M. Evaluation of input current in the critical mode boost PFC converter for distributed power systems. In Proceedings of the 16th Annual IEEE Applied Power Electronics Conference and Exposition (Cat. No. 01CH37181), Anaheim, CA, USA, 4–8 March 2001.
37. Ivanovic, Z.; Blanusa, B.; Knezic, M. Power loss model for efficiency improvement of boost converter. In Proceedings of the 2011 XXIII International Symposium on Information, Communication and Automation Technologies, Sarajevo, Bosnia and Herzegovina, 27–29 October 2011.
38. Rąbkowski, J.; Skoneczny, H.; Kopacz, R.; Trochimiuk, P.; Wrona, G. A Simple Method to Validate Power Loss in Medium Voltage SiC MOSFETs and Schottky Diodes Operating in a Three-Phase Inverter. *Energies* **2020**, *13*, 4773. [CrossRef]
39. Van den Bossche, A.; Valchev, V. Modeling Ferrite Core Losses in Power Electronics. *Int. Rev. Electr. Eng.* **2006**, 14–22. Available online: https://www.praiseworthyprize.org/jsm/index.php?journal=iree&page=issue&op=archive&issuesPage=1#issues (accessed on 21 December 2021).
40. Somkun, S.; Sato, T.; Chunkag, V.; Pannawan, A.; Nunocha, P.; Suriwong, T. Performance Comparison of Ferrite and Nanocrystalline Cores for Medium-Frequency Transformer of Dual Active Bridge DC-DC Converter. *Energies* **2021**, *14*, 2407. [CrossRef]
41. *CLC/FprTS 50549: Part 1-Requirements for Generating Plants to be Connected in Parallel with Distribution Networks—Part 1: Connection to a LV Distribution Network—Generating Plants up to and Including Type B*; European Committee for Electrotechnical Standardization: Brussels, Belgium, 2012. Available online: http://tinyurl.com/TS-50549-1 (accessed on 21 December 2021).